Supplementary Information to "Experimental simulation of Dirac equation in superconducting qubits"

Yu Zhang,[1,2,*] Jianwen Xu,[1,2,*] Zhuang Ma,[1,2,*] Wen Zheng,[1,2]
Dong Lan,[1,2,3,4,†] Xinsheng Tan,[1,2,3,4,‡] and Yang Yu[1,2,3,4,§]

[1]*National Laboratory of Solid State Microstructures, School of Physics, Nanjing University, Nanjing 210093, China*
[2]*Shishan Laboratory, Suzhou Campus of Nanjing University, Suzhou 215000, China*
[3]*Synergetic Innovation Center of Quantum Information and Quantum Physics, University of Science and Technology of China, Hefei, Anhui 230026, China*
[4]*Hefei National Laboratory, Hefei 230088, China*

SUPPLEMENTARY NOTE 1: DEVICE, PARAMETRIC MODULATION, SCHEME FOR CONSTRUCTING HAMILTONIAN

Supplementary Table 1. Parameters

	Q_0	Q_1	Q_2	Q_3
$\omega/2\pi$(GHz)	5.549	5.739	5.673	5.509
$T_1(\mu s)$	8.12	10.00	2.22	6.57
$T_\phi(\mu s)$	1.465	1.158	0.555	0.491

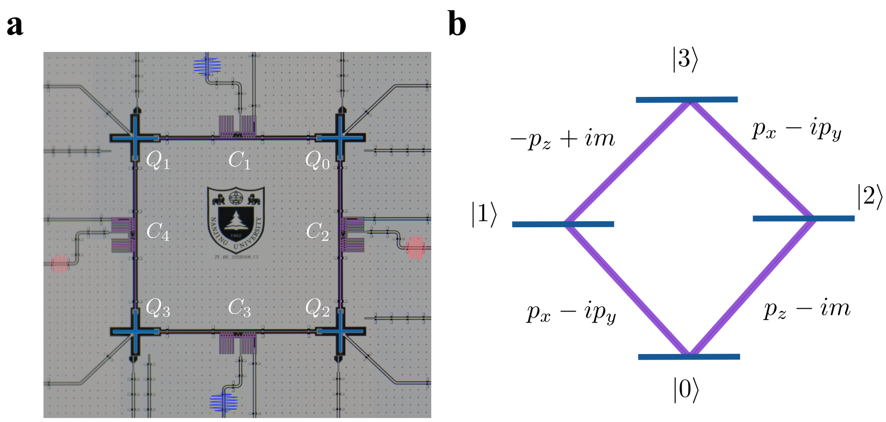

Supplementary Figure 1. **a** Optical image of the device. The cross-shaped capacitor pads of the qubits and the interdigital capacitor pads of tunable couplers are false-coloured blue and purple, respectively. Four sinusoidal parametric flux modulations (demonstrated by blue and red pulses) are applied to four couplers to generate effective couplings. **b** Diamond energy level configuration in the first-excitation manifold of four qubits constructed by parametric modulation. The amplitude and phase of four pulses determine the momentum and mass of the particle; the dynamics of the four-level system simulate the spinor dynamics of the Dirac particle.

The superconducting quantum circuits used in the experiments are shown in Supplementary Figure 1a. The coupling strength between qubit and coupler is $g_{\rm QC}/(2\pi) \approx 100\,\text{MHz}$. Supplementary Table 1 demonstrates the idle frequency ω, T_1 and T_ϕ of four qubits.

The system Hamiltonian in the lab frame is written as

$$
\begin{aligned}
H_{\mathrm{lab}}/\hbar = &\sum_{i=0}^{3}(\omega_{Q_i} a^{\dagger}_{Q_i} a_{Q_i} + \frac{\alpha_{Q_i}}{2} a^{\dagger}_{Q_i} a^{\dagger}_{Q_i} a_{Q_i} a_{Q_i}) + \sum_{i=1}^{4}(\omega_{C_i} a^{\dagger}_{C_i} a_{C_i} + \frac{\alpha_{C_i}}{2} a^{\dagger}_{C_i} a^{\dagger}_{C_i} a_{C_i} a_{C_i}) \\
&+ \sum_{<m,n>} [g_{m,n} a^{\dagger}_{Q_m} a_{C_n} + \mathrm{H.c.}] + \sum_{<r,k>} [g^{0}_{rk} a^{\dagger}_{Q_r} a_{Q_k} + \mathrm{H.c.}]
\end{aligned} \tag{S1}
$$

where $< m, n >$ denotes the set of all qubit-coupler pairs where Q_m is directly connected to coupler C_n, $< r, k >$ denote the set of all qubit pairs (Q_r,Q_k) connected via an intermediate coupler, a and $a^{\dagger}$ are annihilation and creation operator. The frequency and anharmonicity of qubits (couplers) are ω_{Q_i} and α_{Q_i} (ω_{C_i} and α_{C_i}), respectively. The coupling strength between qubit Q_i and its adjacent coupler C_j is $g_{i,j}$. The direct capacitance coupling strength between qubit Q_i and Q_j is g^0_{ij}, much smaller than $g_{i,j}$. All qubits are negatively far detuned from adjacent couplers, $\Delta_{i,j} = \omega_{Q_i} - \omega_{C_j} < 0$, they are operated in the dispersive regime, i.e., $g_{i,j} \ll |\Delta_{i,j}|$. On the one hand, one coupler will introduce an indirect coupling channel between its connected qubits induced by virtual photon exchange. On the other hand, two qubits on the same side of the square are directly coupled with the coupling strength g^0_{ij}. For example, the total effective coupling strength between Q_0 and Q_1 is $J_{01} = g^0_{01} + \frac{g_{0,1} g_{1,1}}{2}(\frac{1}{\Delta_{0,1}} + \frac{1}{\Delta_{1,1}})$. Adiabatically eliminating the coupler, the Lamb-shifted qubit frequency is $\tilde{\omega}_{Q_{0(1)}} = \omega_{Q_{0(1)}} + \frac{(g_{0(1),1})^2}{\Delta_{0(1),1}}$.

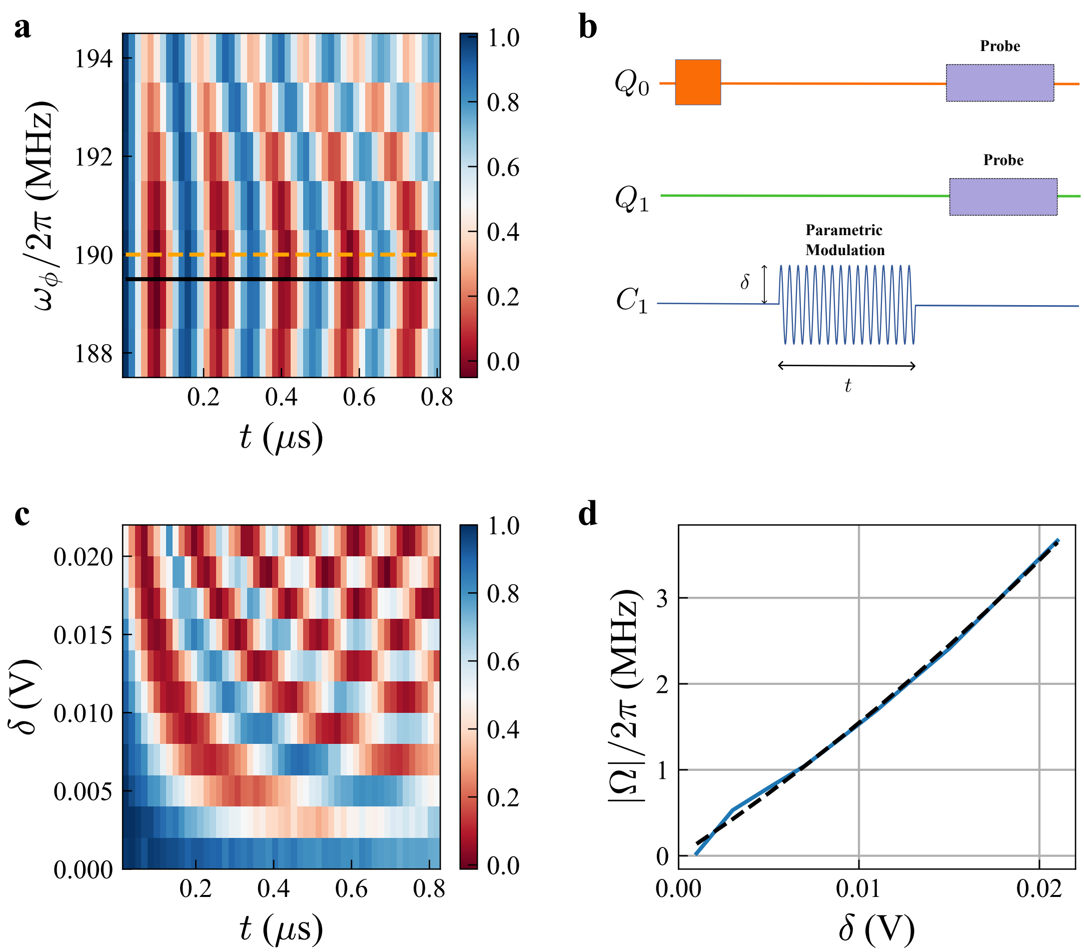

Supplementary Figure 2. The calibration procedure of parametric modulation. **a** The resonance frequency(solid black) is calibrated from the chevron pattern using the pulse sequence shown in **b**. The resonance frequency is slightly different from the detuning of two qubits in the DC bias (dashed orange). **b** The pulse sequence for calibration. **c** Resonance iSWAP interaction for different modulation amplitudes. **d** mapping the pulse amplitude to the effective coupling strength $|\Omega|$.

In order to construct a diamond energy level configuration as shown in Supplementary Figure 1b, we apply four sinusoidal parametric flux modulations on four tunable couplers which have flux dependent frequency $\omega_{C_i}(\phi_i(t))$ and $\phi_i(t) = \Phi_i + \delta_i \cos(\omega_{\phi_i} t + \varphi_i)$ to activate the sideband transition in the first-excitation manifold of four qubits [1–6]. Specifically, two qubits Q_i and Q_j connected by one coupler C_k are detuned from each other, $100\,\mathrm{MHz} < |\omega_{Q_i} - \omega_{Q_j}|/(2\pi) < 300\,\mathrm{MHz}$. The frequency of the parametric modulation $\omega_{\phi_k} = \Delta_{ij,\delta_k}$, where $\Delta_{ij,\delta_k} = \tilde{\omega}_{Q_i} - \tilde{\omega}_{Q_j} + \frac{\delta_k^2}{4}(\frac{\partial^2 \tilde{\omega}_{Q_i}}{\partial \phi_k^2} - \frac{\partial^2 \tilde{\omega}_{Q_j}}{\partial \phi_k^2})$ is the detuning of two qubits effective frequency which is dependent on the amplitude of parametric modulation.

Parametric modulation enables effective coupling between two spectrally detuned qubits. As detailed in Supplementary Figure 2, we calibrate the coupling strength using the Q_0-C_1-Q_1 subsystem. By applying a sinusoidal parametric modulation flux pulse ϕ_1 (amplitude δ_1) to C_1 with initial state $|100\rangle$. We measure the $|100\rangle$ state population as a function of modulation frequency ω_{ϕ_1} and interaction time t. The observed chevron pattern reveals a resonance at 189.5 MHz corresponding to the minimal population exchange rate, yielding a coupling strength $|\Omega|/(2\pi) = 3$ MHz. This resonance frequency deviates from the detuning of two qubits without the flux modulation, $(\tilde{\omega}_{Q_0} - \tilde{\omega}_{Q_1})/(2\pi) = 190$ MHz, since the flux modulation induces AC Stark shift. We calibrate the frequency for different amplitudes. Notably, two adjacent qubits are shifted toward the same direction, and the variation in resonance frequency remains amplitude-insensitive when the modulation amplitude is small.

To simulate the Dirac particle with different momentum and mass, we systematically vary the modulation amplitude and characterize the oscillation speed dependence. This establishes a mapping between the effective coupling strength and the flux pulse amplitude through polynomial fitting. The calibrated relationship enables deterministic calculation of required amplitudes and phases for target mass-momentum parameters. These values are subsequently converted into experimentally generated waveforms.

In the interaction picture, the Hamiltonian can be written as

$$\begin{aligned} H_{\mathrm{eff}}/\hbar =& (\Omega_{01} e^{-i\varphi_1} a_{Q_0}^{\dagger} a_{Q_1}^{-} + \Omega_{02} e^{-i\varphi_2} a_{Q_0}^{\dagger} a_{Q_2}^{-} \\ &+ \Omega_{23} e^{-i\varphi_3} a_{Q_2}^{\dagger} a_{Q_3}^{-} + \Omega_{13} e^{-i\varphi_4} a_{Q_1}^{\dagger} a_{Q_3}^{-}) + \mathrm{H.c.} \end{aligned} \tag{S2}$$

where $\Omega_{01} = \frac{\delta_1}{2}\frac{\partial J_{01}}{\partial \phi_1}$, $\Omega_{02} = \frac{\delta_2}{2}\frac{\partial J_{02}}{\partial \phi_2}$, $\Omega_{23} = \frac{\delta_3}{2}\frac{\partial J_{23}}{\partial \phi_3}$ and $\Omega_{13} = \frac{\delta_4}{2}\frac{\partial J_{13}}{\partial \phi_4}$

The first excitation manifold Hamiltonian in the basis order $(|0\rangle|1\rangle|2\rangle|3\rangle)$ is

$$H = \begin{vmatrix} 0 & \Omega_{01} e^{-i\varphi_1} & \Omega_{02} e^{-i\varphi_2} & 0 \\ \Omega_{01} e^{i\varphi_1} & 0 & 0 & \Omega_{13} e^{-i\varphi_4} \\ \Omega_{02} e^{i\varphi_2} & 0 & 0 & \Omega_{23} e^{-i\varphi_3} \\ 0 & \Omega_{13} e^{i\varphi_4} & \Omega_{23} e^{i\varphi_3} & 0 \end{vmatrix} \tag{S3}$$

As shown in the main text, we rearrange the basis, $|\Psi\rangle = c_0|0\rangle + c_1|1\rangle + c_2|2\rangle + c_3|3\rangle = (c_0\ c_3\ c_2\ c_1)^T$, we get the Dirac Hamiltonian in the supersymmetric representation.

SUPPLEMENTARY NOTE 2: TWO FOLD DEGENERACY

We calculate the eigenvalues λ of H_{s} in the main text. $H_{\mathrm{s}}|\psi\rangle = \lambda|\psi\rangle$

$$\begin{vmatrix} -\lambda & 0 & p_z - im & p_x - ip_y \\ 0 & -\lambda & p_x + ip_y & -p_z - im \\ p_z + im & p_x - ip_y & -\lambda & 0 \\ p_x + ip_y & -p_z + im & 0 & -\lambda \end{vmatrix} = 0 \tag{S4}$$

We have $(m^2 + p_x^2 + p_y^2 + p_z^2 - \lambda^2)^2 = 0$, so both eigenvalues $\lambda = \pm\sqrt{m^2 + p_x^2 + p_y^2 + p_z^2} = \pm E$ of H_{s} have two-fold degeneracy. We assume the eigenstates of E are $|\psi_1\rangle^+$ and $|\psi_2\rangle^+$, the eigenstates of $-E$ are $|\psi_1\rangle^-$ and $|\psi_2\rangle^-$. Any initial state $|\Psi\rangle$ can be decomposed into the superposition of these four states with amplitudes $c_i^{\pm}$. The time evolution of free particles can be expressed as

$$|\Psi\rangle = e^{-iEt}(c_1^+|\psi_1\rangle^+ + c_2^+|\psi_2\rangle^+) + e^{iEt}(c_1^-|\psi_1\rangle^- + c_2^-|\psi_2\rangle^-) \tag{S5}$$

This is an effective two-level dynamic, the same as the Rabi evolution. Therefore, there is no beat pattern in population oscillations for the free Dirac equation.

SUPPLEMENTARY NOTE 3: TOMOGRAPHY

The tomography Hamiltonian is also constructed using parametric modulation and is written as follows after rotating-wave approximation

$$H_{\text{tomo}}/\hbar = \Omega_{01}(t)e^{-i\varphi_m}\sigma_0^-\sigma_1^+ + \Omega_{23}e^{-i\varphi_m}\sigma_2^-\sigma_3^+ + h.c. \tag{S6}$$

where φ_m is the rotating axis in subspace $\{|0\rangle, |1\rangle\}$ and $\{|2\rangle, |3\rangle\}$(These basis notations are the same as the main text). Here we use the basis notation for the total system's Hilbert space, that is $|Q_3Q_2Q_1Q_0\rangle$. We set rotating angle $\int_0^t 2\Omega_{01}(t)dt = \int_0^t 2\Omega_{23}(t)dt = \pi/2$.

We assume the state before the tomography is $|\psi\rangle = c_0|0001\rangle + c_1|0010\rangle + c_2|0100\rangle + c_3|1000\rangle$, then the state after the tomography is written as $|\psi\rangle_f = U_{\text{tomo}}|\psi\rangle = \frac{\sqrt{2}}{2}c_0 - i\frac{\sqrt{2}}{2}e^{i\varphi_m}c_1|0001\rangle + \frac{\sqrt{2}}{2}c_1 - i\frac{\sqrt{2}}{2}e^{-i\varphi_m}c_0|0010\rangle + \frac{\sqrt{2}}{2}c_2 - i\frac{\sqrt{2}}{2}e^{i\varphi_m}c_3|0100\rangle + \frac{\sqrt{2}}{2}c_3 - i\frac{\sqrt{2}}{2}e^{-i\varphi_m}c_2|1000\rangle$, with $U_{\text{tomo}} = e^{-i\int_0^t H_{\text{tomo}}dt/\hbar}$. The density matrix after the tomography is $\rho = |\psi\rangle_{ff}\langle\psi|$, and the reduced density matrices of four qubits are

$$\rho_{Q_0} = \text{tr}_{123}\rho = \begin{bmatrix} |c_2|^2 + |c_3|^2 + 1/2 * |c_0|^2 + 1/2 * |c_1|^2 - \text{Im}(e^{i\varphi_m}c_0^*c_1) & 0 \\ 0 & 1/2 * |c_0|^2 + 1/2 * |c_1|^2 + \text{Im}(e^{i\varphi_m}c_0^*c_1) \end{bmatrix} \tag{S7}$$

$$\rho_{Q_1} = \text{tr}_{023}\rho = \begin{bmatrix} |c_2|^2 + |c_3|^2 + 1/2 * |c_0|^2 + 1/2 * |c_1|^2 + \text{Im}(e^{i\varphi_m}c_0^*c_1) & 0 \\ 0 & 1/2 * |c_0|^2 + 1/2 * |c_1|^2 - \text{Im}(e^{i\varphi_m}c_0^*c_1) \end{bmatrix} \tag{S8}$$

$$\rho_{Q_2} = \text{tr}_{013}\rho = \begin{bmatrix} |c_0|^2 + |c_1|^2 + 1/2 * |c_2|^2 + 1/2 * |c_3|^2 - \text{Im}(e^{i\varphi_m}c_2^*c_3) & 0 \\ 0 & 1/2 * |c_2|^2 + 1/2 * |c_3|^2 + \text{Im}(e^{i\varphi_m}c_2^*c_3) \end{bmatrix} \tag{S9}$$

$$\rho_{Q_3} = \text{tr}_{012}\rho = \begin{bmatrix} |c_0|^2 + |c_1|^2 + 1/2 * |c_2|^2 + 1/2 * |c_3|^2 + \text{Im}(e^{i\varphi_m}c_2^*c_3) & 0 \\ 0 & 1/2 * |c_2|^2 + 1/2 * |c_3|^2 - \text{Im}(e^{i\varphi_m}c_2^*c_3) \end{bmatrix} \tag{S10}$$

Then we measure $\langle\sigma_z\rangle$ of four qubits. $\langle\sigma_z\rangle_0 = \text{tr}(\sigma_z\rho_{Q_0}) = |c_2|^2 + |c_3|^2 - 2\text{Im}(e^{i\varphi_m}c_0^*c_1)$, $\langle\sigma_z\rangle_1 = \text{tr}(\sigma_z\rho_{Q_1}) = |c_2|^2 + |c_3|^2 + 2\text{Im}(e^{i\varphi_m}c_0^*c_1)$, $\langle\sigma_z\rangle_2 = \text{tr}(\sigma_z\rho_{Q_2}) = |c_0|^2 + |c_1|^2 - 2\text{Im}(e^{i\varphi_m}c_2^*c_3)$, $\langle\sigma_z\rangle_3 = \text{tr}(\sigma_z\rho_{Q_3}) = |c_0|^2 + |c_1|^2 + 2\text{Im}(e^{i\varphi_m}c_2^*c_3)$. Measurement result $\langle\sigma_z\rangle_n^m$ represents the expectation value of Q_n after the tomography with phase $\varphi_m = m\pi/2$, $m = 0, 1, 2, 3$. According to the definition of v_x and v_y, we have $v_x = (-\langle\sigma_z\rangle_0^1 + \langle\sigma_z\rangle_0^3 + \langle\sigma_z\rangle_1^1 - \langle\sigma_z\rangle_1^3 - \langle\sigma_z\rangle_2^1 + \langle\sigma_z\rangle_2^3 + \langle\sigma_z\rangle_3^1 - \langle\sigma_z\rangle_3^3)/4$ and $v_y = (-\langle\sigma_z\rangle_0^0 + \langle\sigma_z\rangle_0^2 + \langle\sigma_z\rangle_1^0 - \langle\sigma_z\rangle_1^2 - \langle\sigma_z\rangle_2^0 + \langle\sigma_z\rangle_2^2 + \langle\sigma_z\rangle_3^0 - \langle\sigma_z\rangle_3^2)/4$.

SUPPLEMENTARY NOTE 4: ZBW AND COMMUTATION RELATION

The Dirac Hamiltonian of free spin 1/2 particle is $H_{\text{D}} = c\boldsymbol{\alpha} \bullet \mathbf{p} + \beta mc^2$. We have velocity operator $\frac{d}{dt}x(t) = \frac{1}{i\hbar}[x(t), H_{\text{D}}] = c\alpha_1(t)$, $\frac{d}{dt}y(t) = \frac{1}{i\hbar}[y(t), H_{\text{D}}] = c\alpha_2(t)$, $\frac{d}{dt}z(t) = \frac{1}{i\hbar}[z(t), H_{\text{D}}] = c\alpha_3(t)$, and the time derivative of velocity operator is $\frac{d}{dt}c\alpha_i(t) = \frac{1}{i\hbar}[c\alpha_i(t), H_{\text{D}}] = e^{iH_{\text{D}}t}\frac{1}{i\hbar}[c\alpha_i, H_{\text{D}}]e^{-iH_{\text{D}}t} = e^{iH_{\text{D}}t}\frac{1}{i\hbar}(\{c\alpha_i, H_{\text{D}}\} - 2H_{\text{D}}c\alpha_i)e^{-iH_{\text{D}}t}$, so

$$\frac{d}{dt}c\alpha_i(t) = e^{iH_{\text{D}}t}\frac{1}{i\hbar}(2c^2p_i - 2H_{\text{D}}c\alpha_i)e^{-iH_{\text{D}}t} = 2\frac{i}{\hbar}H_{\text{D}}F_i(t) \tag{S11}$$

We have $F_i(t) = c\alpha_i(t) - c^2p_iH_{\text{D}}^{-1}$. $F_i = c\alpha_i - c^2p_iH_{\text{D}}^{-1}$ is anticommutes with H_{D}, $F_iH_{\text{D}} = -H_{\text{D}}F_i$, so $F_i(t) = e^{2iH_{\text{D}}t/\hbar}F_i$. Integrating S11, we will get $c\alpha_i(t) = c^2p_iH_{\text{D}}^{-1} + F_i(t)$, where $c^2p_iH_{\text{D}}^{-1}$ is classical velocity operator, $F_i(t)$ is the velocity oscillation. If $[\alpha_i, H_{\text{D}}] \neq 0$, we may observe Zitterbewegung in the i direction. We prepare the initial state as $|\psi\rangle = |0\rangle$ as stated in the main text. Furthermore, we analytically calculate the expectation

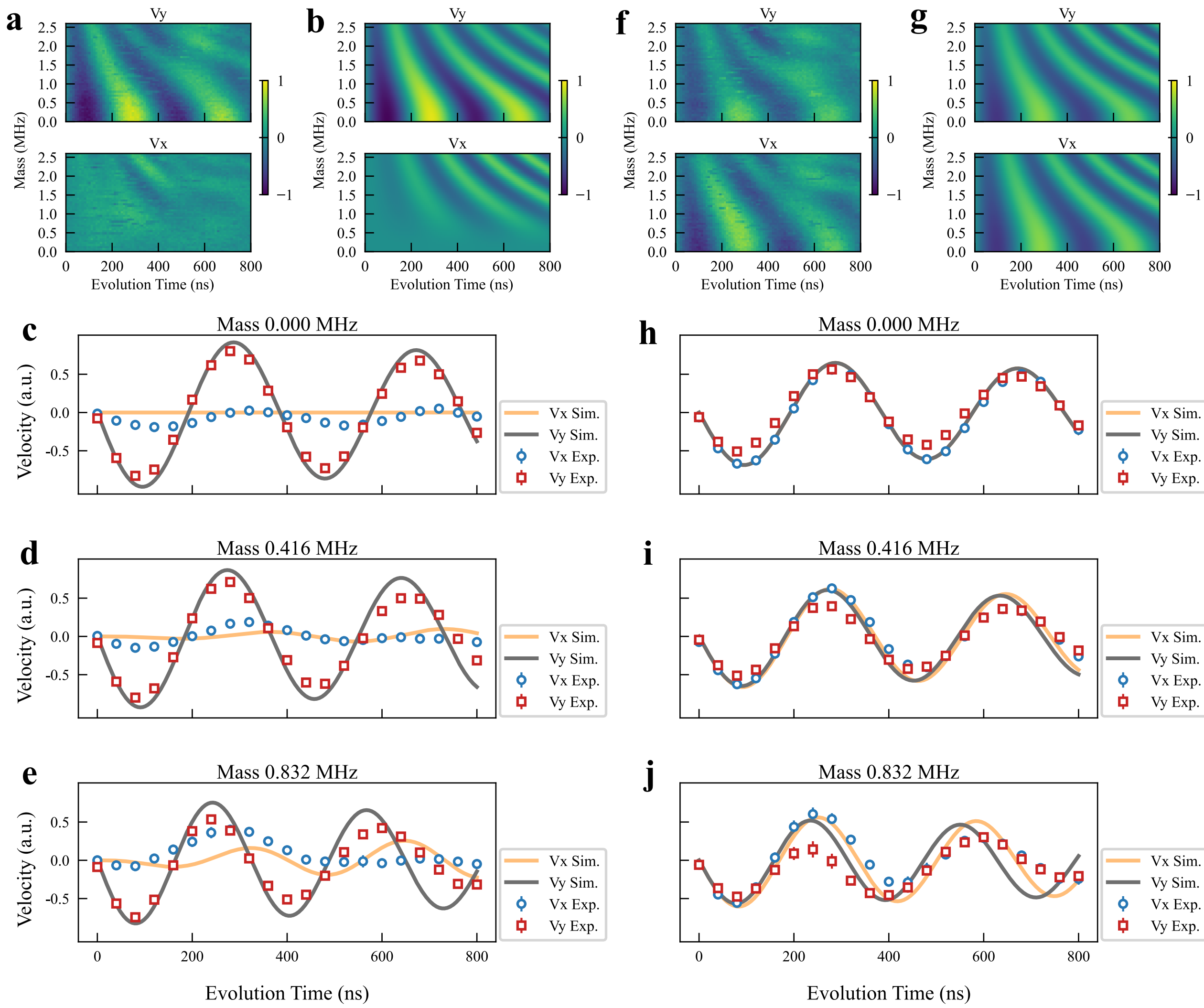

Supplementary Figure 3. Expected values of velocity operator and Zitterbewegung. **a,b** Experimental(**a**) and simulation(**b**) results of velocity in the x and y directions are demonstrated. The momentum is $\mathbf{p} = (1.3\,\text{MHz}, 0, 0)$, and the ZBW, which originated from the interference between the positive and negative energy components, can be observed only in the x direction for the initial state $|0\rangle$. **c,d,e** Velocities for three specific masses. The speed of oscillation increases with the mass. (**f,g,h,i,j**) are the same with (**a,b,c,d,e**) except different momentum $\mathbf{p} = (1.3/\sqrt{2}\,\text{MHz}, -1.3/\sqrt{2}\,\text{MHz}, 0)$.

value of three velocities according to the initial state. We find $v_x(t) = \langle\psi|c\alpha_x(t)|\psi\rangle = \frac{cp_y \sin(\frac{2ct\sqrt{c^2m^2+p_x^2+p_y^2+p_z^2}}{\hbar})}{\sqrt{c^2m^2+p_x^2+p_y^2+p_z^2}}$, $v_y(t) = \langle\psi|c\alpha_y(t)|\psi\rangle = -\frac{cp_x \sin(\frac{2ct\sqrt{c^2m^2+p_x^2+p_y^2+p_z^2}}{\hbar})}{\sqrt{c^2m^2+p_x^2+p_y^2+p_z^2}}$ and $v_z(t) = \langle\psi|c\alpha_z(t)|\psi\rangle = \frac{c^2 m \sin(\frac{2ct\sqrt{c^2m^2+p_x^2+p_y^2+p_z^2}}{\hbar})}{\sqrt{c^2m^2+p_x^2+p_y^2+p_z^2}}$. As shown in Supplementary Figure 3, With $\mathbf{p} = (1.3\,\text{MHz}, 0, 0)$, $p_y = 0$ means the expectation value of α_x is zero without rapid oscillation. When $\mathbf{p} = (1.3/\sqrt{2}\,\text{MHz}, -1.3/\sqrt{2}\,\text{MHz}, 0)$, oscillation pattern of v_x and v_y are the same.

We also analytically calculate the results of ZBW if we prepare another initial state $|\psi\rangle = (|0\rangle + |1\rangle)/\sqrt{2}$. $v_x(t) = \langle\psi|c\alpha_x(t)|\psi\rangle = \frac{c[p_x^2+(c^2m^2+p_y^2+p_z^2)\cos(\frac{2ct\sqrt{c^2m^2+p_x^2+p_y^2+p_z^2}}{\hbar})]}{c^2m^2+p_x^2+p_y^2+p_z^2}$, $v_y(t) = \langle\psi|c\alpha_y(t)|\psi\rangle = \frac{2cp_xp_y \sin^2(\frac{ct\sqrt{c^2m^2+p_x^2+p_y^2+p_z^2}}{\hbar})}{c^2m^2+p_x^2+p_y^2+p_z^2}$ and $v_z(t) = \langle\psi|c\alpha_z(t)|\psi\rangle = \frac{c[p_xp_z - p_xp_z\cos(\frac{2ct\sqrt{c^2m^2+p_x^2+p_y^2+p_z^2}}{\hbar}) + cm\sqrt{c^2m^2+p_x^2+p_y^2+p_z^2}\sin(\frac{2ct\sqrt{c^2m^2+p_x^2+p_y^2+p_z^2}}{\hbar})]}{c^2m^2+p_x^2+p_y^2+p_z^2}$.

If the initial state is an eigenstate of Dirac Hamiltonian, with positive or negative eigenvalue, this condition cannot endow the particle both positive and negative component, we cannot observe ZBW in any direction. For instance, we prepare initial state $|\psi\rangle = \frac{i(p_x-ip_y)}{\sqrt{2}\sqrt{c^2m^2+p_x^2+p_y^2+p_z^2}}|0\rangle + \frac{-i}{\sqrt{2}}|1\rangle + \frac{cm-ip_z}{\sqrt{2}\sqrt{c^2m^2+p_x^2+p_y^2+p_z^2}}|3\rangle$, and

$H_{\rm D}|\psi\rangle = -c\sqrt{c^2m^2+p_x^2+p_y^2+p_z^2}|\psi\rangle$, we will get $v_i(t) = -\frac{cp_i}{\sqrt{c^2m^2+p_x^2+p_y^2+p_z^2}}$, where i=x,y,z.

SUPPLEMENTARY NOTE 5: READOUT ERROR MITIGATION

The selection of the coupler's DC bias Φ_i involves multiple considerations. In the following analysis, we take Q_0-C_1-Q_1 as an example. The first factor is the derivative of the coupler's frequency with respect to the flux (the slope $\frac{\partial\omega_{C_1}}{\partial\phi_1}$) which determines the effective qubit-qubit coupling achievable through parametric modulation, $\frac{\delta_1}{2}\frac{g_{0,1}g_{1,1}}{2}\frac{\partial\omega_{C_1}}{\partial\Phi_1}[\frac{1}{(\omega_0-\omega_{C_1}(\Phi))^2}+\frac{1}{(\omega_1-\omega_{C_1}(\Phi))^2}]$. The second factor is that the coupler needs to avoid certain frequencies. For example, it should be sufficiently detuned from qubit frequencies to preserve dispersive conditions. Additionally, it must avoid resonance with its own readout resonator and prevent potential sideband transitions between the qubit and the coupler. The third factor is that the coupler's frequency governs the XY coupling $J_{0,1}$ between qubits, to avoid affecting the coupling achieved through parametric modulation, it is ideally chosen at the switch-off $\omega_{C_1}^{\rm off}$ which turns off the coupling. However, since the switch-off bias for this sample design corresponds to a coupler frequency around 8 GHz, where the slope is small, it is not suitable for this kind of parametric modulation in quantum simulation.

Therefore, in the experiments, we choose the coupler's idle frequency to be 500 MHz below its readout resonator frequency, ensuring that the modulation amplitude does not exceed the detuning between the coupler's idle frequency and the readout cavity frequency, and we slightly adjust the qubits' idle frequency downwards for dispersive conditions. Although residual coupling persists, the large qubit-qubit detuning (exceeds 120 MHz) renders it dynamically negligible under the rotating-wave approximation. Nevertheless, this static coupling still affects the readout, we need to optimize the probe's frequency and amplitude and qubits' frequency to minimize readout crosstalk as much as possible.

In the Schwinger effect experiment, experimental observations reveal residual readout crosstalk. Initializing the system in $|0\rangle$, the dynamics remain confined to the subspace $\{|0\rangle,|1\rangle\}$ due to massless regime ($m=0$) that decouples the subspace $\{|2\rangle,|3\rangle\}$. However, after the evolution, the measurements yield $P_{0,1}\approx 1$ (the population of $\{|0\rangle,|1\rangle\}$) for target subspace, yet $P_{2,3}\approx 0.2$ (the population in $\{|2\rangle,|3\rangle\}$) indicates non-negligible readout crosstalk. The crosstalk impact of $P_{2,3}$ on $P_{0,1}$ is small. To mitigate the readout error, we define the crosstalk matrix as $M=\begin{pmatrix}1 & \epsilon_2\\ \epsilon_1 & 1\end{pmatrix}$, where ϵ_1 is obtained from the raw data of the $P_{2,3}$ for m near zero, and calculate the real populations: $\begin{pmatrix}P_{0,1}^{\rm real}\\ P_{2,3}^{\rm real}\end{pmatrix} = M^{-1}\begin{pmatrix}P_{0,1}^{\rm exp}\\ P_{2,3}^{\rm exp}\end{pmatrix}$. We then use $P_{2,3}^{\rm real}$ to calculate $P_{0,1}^{\rm real}$ based on the population normalization condition. After applying this error mitigation, we find that the experiment data is more consistent with the numerical simulation results.

* These authors contributed equally to this work.
† Land@nju.edu.cn
‡ tanxs@nju.edu.cn
§ yuyang@nju.edu.cn
[1] McKay, D. C. *et al.* Universal gate for fixed-frequency qubits via a tunable bus. *Phys. Rev. Appl.* **6**, 064007 (2016). URL https://link.aps.org/doi/10.1103/PhysRevApplied.6.064007.
[2] Roth, M. *et al.* Analysis of a parametrically driven exchange-type gate and a two-photon excitation gate between superconducting qubits. *Phys. Rev. A* **96**, 062323 (2017). URL https://link.aps.org/doi/10.1103/PhysRevA.96.062323.
[3] Reagor, M. *et al.* Demonstration of universal parametric entangling gates on a multi-qubit lattice. *Science Advances* **4**, eaao3603 (2018). URL https://www.science.org/doi/abs/10.1126/sciadv.aao3603.
[4] Ganzhorn, M. *et al.* Gate-efficient simulation of molecular eigenstates on a quantum computer. *Phys. Rev. Appl.* **11**, 044092 (2019). URL https://link.aps.org/doi/10.1103/PhysRevApplied.11.044092.
[5] Mundada, P., Zhang, G., Hazard, T. & Houck, A. Suppression of qubit crosstalk in a tunable coupling superconducting circuit. *Phys. Rev. Appl.* **12**, 054023 (2019). URL https://link.aps.org/doi/10.1103/PhysRevApplied.12.054023.
[6] Ganzhorn, M. *et al.* Benchmarking the noise sensitivity of different parametric two-qubit gates in a single superconducting quantum computing platform. *Phys. Rev. Res.* **2**, 033447 (2020). URL https://link.aps.org/doi/10.1103/PhysRevResearch.2.033447.